GEOMETRIC AND CONVENTIONAL CONTRIBUTIONS TO SUPERFLUID WEIGHT IN THE MINIMAL MODELS FOR SUPERCONDUCTING FLAT BANDS INDUCED BY DOPING*

Wojciech Brzezicki

Institute of Theoretical Physics, Jagiellonian University
S. Łojasiewicza 11, 30-348 Kraków, Poland

Timo Hyart

Computational Physics Laboratory, Physics Unit
Faculty of Engineering and Natural Sciences, Tampere University
FI-33014 Tampere, Finland
and
BA5502 ProperTune ICME, VTT Technical Research Centre of Finland Ltd
Kuopio, Finland

Received 13 March 2026, accepted 16 March 2026, published online 15 May 2026

The density functional theory calculations and tight-binding models for the doped lead apatite (and other materials in the same symmetry group) support flat bands, which could be susceptible to the emergence of various correlated phases including superconductivity. We develop a theory for the geometric contribution of the superfluid weight arising from the momentum-space topology of the Bloch wave functions of these flat bands, and we compare our results to the paradigmatic case of s-wave superconductivity on an isolated topological flat band. We show that, in contrast to the standard paradigm of flat-band superconductivity, there does not exist any lower bound for the superfluid weight in these models. Moreover, although the nontrivial quantum geometries of the normal-state bands are the same when the superconductivity appears in the ferromagnetic and paramagnetic phases, the emerging superconducting phases have very different superfluid weights. In the case of superconductivity appearing on the spin-polarized bands, the superfluid weight varies a lot as a function of model parameters. On the other hand, if the superconductivity emerges in the paramagnetic phase, the superfluid weight is robustly large and it contains a significant geometric component.

DOI:10.5506/APhysPolB.57.5-A13

* Presented at the Concepts in Strongly Correlated Quantum Matter Conference (CSCQM), Kraków, Poland, 20–22 November, 2025.

1. Introduction

The initial reports of high-temperature superconductivity in copper-doped lead apatite [1, 2] sparked an active debate and numerous replication attempts, which initially yielded only partial success [3, 4]. However, later experimental studies showed that the system is an insulator rather than a superconductor [5, 6], and attributed the observed resistivity drop to a first order structural phase transition of Cu_2S impurities [7, 8]. On the other hand, some recent studies have shown that specific chemical modifications, such as sulfur doping, might tune these structures to successfully host superconducting states [9–11] by driving the system into paramagnetic state. In this paper, we explore the models proposed for the doping-induced bands in this symmetry class of materials purely from the theoretical viewpoint without specifically focusing on any particular material.

Density functional theory (DFT) calculations suggest that these materials support spin-polarized bands at the Fermi level [12–16], and due to their small bandwidth, they are called flat bands. It was proposed that the flat bands could support correlated phases at high temperature [12], because the large density of states can lead to an exponential enhancement of the critical temperature [17]. However, since the kinetic energy is quenched, the flat bands are expected to be susceptible to various instabilities, which may lead to the appearance of magnetic, orbital or superconducting order [18–23] as has been observed in quantum Hall systems [18, 19], moiré superlattices [24–34], and other flat-band systems [35, 36]. One of the most exciting aspects of the models for doped lead apatite is that, in contrast to the flat-band systems studied experimentally so far, the flat bands in this system are three-dimensional, allowing the possibility of more stable correlated phases [23, 37]. However, the understanding of the details of the competition of the order parameters as a function of external parameters and structural properties of the samples, as well as the experimental advances in the sample fabrication techniques to achieve robust control of the appearing order parameters, are major challenges for the future investigations. The guiding principle is that one should avoid being at half-filling of the flat bands if one wants to realize superconducting phases because the change of the filling away from the exact half-filling is more detrimental to the other types of order parameters than to the superconductivity [20, 23]. In the spin-polarized case, the two spin-polarized flat bands are half-filled on average (*i.e.* the total filling of the two bands is 1) because the corresponding bands in the other spin sector are far below the Fermi level and fully occupied, but in the paramagnetic phase of this material, the two flat bands in each spin sector are 3/4 filled on average (*i.e.* the total filling of the four bands is 3). Additionally, from the two flat bands, the upper one has a significantly larger bandwidth [12–16], and another important guid-

ing principle is that the larger bandwidth also favors superconducting order parameter relative to the other order parameters. Thus, both guiding principles suggest that the paramagnetic phase is a more favorable environment to support superconductivity, but this comes with the cost of lowering the overall magnitude of the critical temperature of the correlated phases, which is expected to reach the maximum at half-filling [20, 23] and it also decreases with the increasing bandwidth [17].

In order to understand the potential of the proposed phases for superconductivity, the key property which should be studied is the superfluid weight D_s, which captures the ability of a material to support supercurrent and the Meissner effect [38, 39]. For conventional superconductors originating from the metallic state, one has the well-known result $D_s = e^2 n/m^*$, where n is the electronic density and m^* the effective mass [38]. However, the experimental observations of superconductivity in twisted bilayer graphene [24, 26–29] and other flat-band systems [32–36], where the effective mass m^* is large and one would expect D_s to be small, demonstrate that there must also exist other contributions to the superfluid weight. Indeed, it has been theoretically found that, besides the band dispersion, also the quantum geometry of the Bloch wave functions contributes to the superfluid weight [18, 22, 40–46]. In particular, in the paradigmatic case of a well-isolated flat band supporting time-reversal invariant s-wave singlet superconductivity with spin-rotation symmetry around the z-axis, the superfluid weight originates purely from the quantum geometry and there exists a lower bound determined by the integral of the absolute value of the Berry curvature [40, 41]. This means that if this type of system supports spin-up and spin-down flat bands carrying opposite spin-Chern numbers there exists a lower bound for D_s given by the value of the Chern number [40]. Similar lower bounds can also be obtained when the bands are characterized by other topological invariants [43], and significant geometric contributions have also been found in three dimensional systems [23] and disordered systems [47].

In this paper, we study the geometric and conventional contributions to superfluid weight in the minimal models for doping-induced flat bands in the lead apatite materials class [48–51]. These models support nontrivial momentum space topologies [48, 51], and therefore there could exist a significant geometric contribution to the superfluid weight. However, the studied models fall outside the standard paradigms of flat-band superconductivity because they can break all possible assumptions required for the existence of the universal lower bounds determined by topological invariants:

(i) even though the bandwidths are small, the bands are not perfectly flat,

(ii) the bands are not well-isolated and depending on the tight-binding parameters, there can even exist topologically protected Weyl points

which force the bands to be degenerate at certain momentum values [48, 51],

(iii) according to the DFT predictions, the system does not obey time-reversal symmetry but instead, the flat bands are expected to be spin-polarized [12–16], and

(iv) the spin-polarized bands cannot support singlet superconductivity.

We find that due to these reasons, there does not exist any kind of lower bound for the superfluid weight in this kind of system. In particular, we show that the superfluid weight can even be negative in the proposed models, indicating instability of the superconducting state.

We perform a comprehensive study of the behavior of the superfluid weight in the candidate models by considering both the interorbital-pairing superconductivity in the spin-polarized phase [50] and the s-wave singlet superconductivity in the paramagnetic phase. Although the paramagnetic phase is not supported by the DFT calculations, there could exist competition between ferromagnetism and superconductivity so that the transition to the superconducting phase would be accompanied by the disappearance of the spin polarization. Additionally, we also consider the effects of the spin-orbit coupling [51] and mirror-symmetry-breaking terms [48] on the normal state, superconducting state and superfluid weight. Interestingly, we find that although the nontrivial quantum geometries of the normal-state bands are the same when the superconductivity appears in the ferromagnetic and paramagnetic phases, the emerging superconducting phases have very different superfluid weights. In the case of superconductivity appearing on the spin-polarized bands, the superfluid weight varies a lot as a function of model parameters, whereas in the absence of spin polarization, the singlet-superconductivity has a robust and large superfluid weight originating from the quantum geometry. In order to better understand the effects caused by the coupling of the bands on the superfluid weight, we introduce a perturbation to our Hamiltonian which enables the realization of the superconductivity on an isolated flat band, and study the behavior of the superfluid weight when the system is tuned from this ideal paradigmatic limit to the models proposed for doped lead apatite.

2. Normal-state Hamiltonian

Our starting point is the low-energy Hamiltonian for d_{xz} and d_{yz} orbitals of Cu atoms (or other dopants depending on the material) forming a triangular lattice shown in Fig. 1 (a). It can be written as [48]

$$
\begin{aligned}
H_0(\boldsymbol{k}) &= \sum_{\nu=0}^{4} d_\nu(\boldsymbol{k})\sigma_\nu \,, \\
d_0(\boldsymbol{k}) &= \bar{t}_0 \left[-\frac{1}{4} \sum_{i=1}^{3} \cos(\boldsymbol{k}\cdot\boldsymbol{b}_i) - \frac{3}{2} \right] - 2t_z \cos k_z \,, \\
d_1(\boldsymbol{k}) &= \frac{\sqrt{3}t_0}{4} \left[\cos(\boldsymbol{k}\cdot\boldsymbol{b}_1) - \cos(\boldsymbol{k}\cdot\boldsymbol{b}_2) \right] \,, \\
d_2(\boldsymbol{k}) &= \frac{\sqrt{3}\hat{t}_0}{4} \sum_{i=1}^{3} \sin(\boldsymbol{k}\cdot\boldsymbol{b}_i) \,, \\
d_3(\boldsymbol{k}) &= \frac{t_0}{4} \left[\cos(\boldsymbol{k}\cdot\boldsymbol{b}_1) + \cos(\boldsymbol{k}\cdot\boldsymbol{b}_2) - 2\cos(\boldsymbol{k}\cdot\boldsymbol{b}_3) \right] \,,
\end{aligned} \tag{1}
$$

where the hoppings between the Cu orbitals, t_0, $\hat{t}_0$, $\bar{t}_0$, and t_z, are mediated by the p_x and p_y orbitals of O atoms [see Fig. 1 (a)], and the lattice vectors $\boldsymbol{b}_i$ satisfy: $\boldsymbol{b}_1 = -\sqrt{3}\hat{e}_x/2 + 3\hat{e}_y/2$, $\boldsymbol{b}_2 = -\sqrt{3}\hat{e}_x/2 - 3\hat{e}_y/2$, $\boldsymbol{b}_3 = \sqrt{3}\hat{e}_x$. The chemical potential μ should be determined so that the filling of the bands is correct. This nearest-neighbor hopping model can be obtained from symmetry considerations by requiring that the Hamiltonian satisfies spinless time-reversal symmetry (TRS)

$$
H_0^T(-\boldsymbol{k}) = H_0(\boldsymbol{k}) \,, \tag{2}
$$

a three-fold rotation symmetry

$$
U^\dagger H_0 \left(\boldsymbol{b}_1\cdot\boldsymbol{k} \to \boldsymbol{b}_2\cdot\boldsymbol{k} \to \boldsymbol{b}_3\cdot\boldsymbol{k} \to \boldsymbol{b}_1\cdot\boldsymbol{k} \right) U = H_0(\boldsymbol{k}) \,, \tag{3}
$$

where

$$
U = \begin{pmatrix} \cos(2\pi/3) & \sin(2\pi/3) \\ -\sin(2\pi/3) & \cos(2\pi/3) \end{pmatrix} \,, \tag{4}
$$

a spinless in-plane mirror symmetry

$$
\sigma_z H_0(-k_x, k_y, k_z)\sigma_z = H_0(k_x, k_y, k_z) \,, \tag{5}
$$

and an out-of-plane mirror symmetry

$$
H_0(k_x, k_y, -k_z) = H_0(k_x, k_y, k_z) \,. \tag{6}
$$

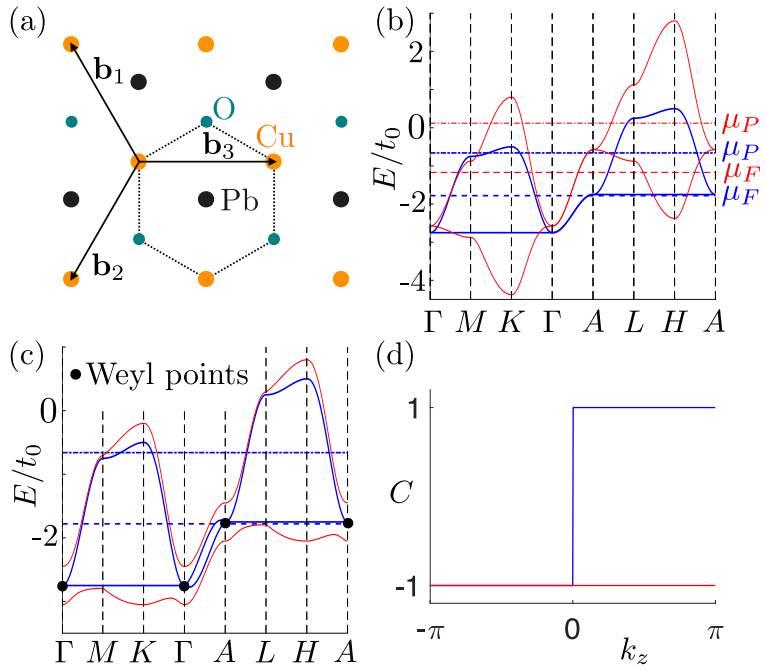

Fig. 1. (a) The lattice structure showing the positions of the most relevant atoms for the low-energy theory. The flat bands originate mostly from the d_{xz} and d_{yz} orbitals of Cu atoms forming a triangular lattice in (x, y)-planes. Together with the Pb atoms, the Cu atoms form honeycomb lattice, where all atoms are in the same layer. The O atoms, which are located in a different layer, form a buckled honeycomb lattice together with Cu atoms. The p_x and p_y orbitals of O atoms mediate hoppings between the Cu orbitals. The full 3D structure is obtained by stacking these layers. (b) The band structure of Hamiltonian (1) with flat-band parameters (blue) and H–M parameters (red), given in Table 1, along the high-symmetry path in the Brillouin zone. The Fermi levels in the ferromagnetic ($\mu_{\rm F}$) and paramagnetic ($\mu_{\rm P}$) phases are shown with the blue and red dashed lines for the two sets of parameters. Here, $\Gamma = (0, 0, 0)$, $M = (0, 2\pi/3, 0)$, $K = (2\pi/(3\sqrt{3}), 2\pi/3, 0)$, $A = (0, 0, \pi)$, $L = (0, 2\pi/3, \pi)$, $H = (2\pi/(3\sqrt{3}), 2\pi/3, \pi)$. (c) Effects of mirror-symmetry-breaking hopping ($t_{z-} = t_0/12$, blue line) and spin-orbit coupling ($\lambda = 0.3t_0$, red line) on the band structure obtained with the flat-band parameters. The double Weyl points in the mirror-symmetry-broken case appear at Γ and A. (d) The Chern number of the lower band as a function of k_z in the presence of mirror-symmetry-breaking term ($t_{z-} = t_0/12$, blue line) and spin-orbit coupling ($\lambda = 0.3t_0$, red line).

Two additional in-plane mirror symmetries can be obtained by combining (5) with the rotation symmetry. If one considers only the dominant hopping paths along the bond directions, the hoppings satisfy $t_0 = \hat{t}_0 = \bar{t}_0$. This was shown in Ref. [50] for hoppings mediated by the d_{xz} and d_{yz} orbitals of Pb atoms, but it remains true also in a more realistic model where the hoppings are mediated by the p_x and p_y orbitals of O atoms. Interestingly, for this relation between the hopping amplitudes, the energy of the lower band is given by [50]

$$\varepsilon_1(\boldsymbol{k}) = -\frac{9}{4}t_0 - 2t_z \cos k_z \,, \tag{7}$$

producing a perfectly flat band as a function of k_x and k_y [50]. In Table 1, we refer to these hopping amplitudes as the flat-band parameters, where we have additionally chosen $t_z = 0.25t_0$ in agreement with Ref. [50]. According to the DFT calculations [12–16], the hopping amplitudes of the copper-doped lead apatite do not satisfy this relationship, leading to weak dispersion as a function of k_x and k_y, which is illustrated for the parameters proposed by Hirschmann and Mitscherling [48] (see H–M parameters in Table 1) in Fig. 1 (b). It should be emphasized that the energy scale is $t_0 \approx 30$ meV [48], so that the bands are always relatively flat.

Table 1. Table of parameter values used for the calculations in this paper. Here, μ_{F} (μ_{P}) is the value of the chemical potential in the ferromagnetic (paramagnetic) phase. The hopping parameter $t_0 \approx 30$ meV.

Parameter	Flat-band parameters	H–M parameters
$\bar{t}_0/t_0$	1	0.7
$\hat{t}_0/t_0$	1	2.3
t_z/t_0	0.25	0.5
μ_{F}/t_0	−1.78	−1.17
μ_{P}/t_0	−0.66	0.12

There also exist two important corrections to the Hamiltonian given in Eq. (1). The O atoms break the mirror symmetries (5) and (6) [12–16, 48, 49], resulting in a mirror-symmetry-breaking hopping term between the Cu orbitals [48]

$$H_{\mathrm{mb}}(\boldsymbol{k}) = -2t_{z-} \sin k_z \; \sigma_2 \,. \tag{8}$$

Notice that this perturbation obeys the spinless TRS (2) and three-fold rotational symmetry (3). Additionally, the spin-orbit coupling cannot be neglected because the unit cell contains a large number of Pb atoms [52]

and also the Cu is known to have spin-orbit coupling comparable to tight-binding hopping parameters in this model [53]. Similarly, as in the recent work [51], we introduce the spin-orbit coupling with the Hamiltonian

$$H_{\mathrm{so}}(\boldsymbol{k}) = \lambda\sigma_2\,. \tag{9}$$

This Hamiltonian breaks the spinless TRS (2) and in-plane mirror (5) symmetries. Although the spin-orbit coupling does not break the true TRS and in-plane mirror symmetries, the spinless versions of these symmetries are broken. From the physics viewpoint, this means that in the spin-polarized phase, there is no TRS or in-plane mirror symmetries because the combination of spin-splitting field and spin-orbit coupling breaks these symmetries. In the paramagnetic phase, this perturbation preserves spinful TRS and spinful mirror symmetries (see below).

The two types of symmetry-breaking terms (8) and (9) lead to different kinds of momentum-space topologies of the normal-state Hamiltonian. The Hamiltonian (8) introduces double Weyl points at Γ and A [48] as shown in Fig. 1 (c), so that the Chern number, calculated for the lower band over the (k_x, k_y)-plane with fixed k_z, satisfies [48]

$$C = \begin{cases} -1\,, & -\pi < k_z < 0 \\ +1\,, & 0 < k_z < \pi \end{cases} \tag{10}$$

as shown in Fig. 1 (d). Introducing the spin-orbit coupling term in the presence of mirror-breaking term moves the Weyl points away from the Γ and A points so that they finally merge and annihilate each other at $\lambda = 2t_{z-}$ [51]. If $\lambda > 2t_{z-}$ so that the Weyl points have been annihilated, the Chern number satisfies

$$C = -1\,, \quad \text{for all } k_z \tag{11}$$

as shown in Fig. 1 (d).

2.1. Ferromagnetic phase

In the ferromagnetic phase, favored by the DFT calculations [12–16], the two spin-↑ flat bands are described by a Hamiltonian

$$H_{\uparrow}(\boldsymbol{k}) = H_0(\boldsymbol{k}) + H_{\mathrm{mb}}(\boldsymbol{k}) + H_{\mathrm{so}}(\boldsymbol{k}) - \mu_{\mathrm{F}}\,\sigma_0\,, \tag{12}$$

and the spin-↓ are far below the Fermi level and fully occupied, so that they do not influence the low-energy theory close to the Fermi level at all. Therefore, the spin-↑ orbitals are on average half-filled, so that the total filling factor of the two bands of the Hamiltonian (12) is 1. This means that the Fermi level μ_{F} in the system is in-between the Weyl point energies

as shown in Fig. 1 (c), so that the system is ideal for observing the Fermi arcs protected by the spin-Chern number $C_\uparrow = C$, where C is given by Eq. (10). Importantly, the system remains topologically nontrivial if the spin-orbit coupling causes the annihilation of the Weyl points because the spin-Chern number is $C_\uparrow = C = -1$ for all k_z, giving rise to surface states which resemble the Fermi arcs of the Weyl semimetal phase in the surface density of states but they have the same chirality for all values of k_z, so their effect on transport properties is expected to be different. In principle, such kind of chiral currents may repel the magnetic field and cause diamagnetism even in the absence of superconductivity. This could happen because in the absence of a magnetic field, the sample will likely contain domains where the magnetization direction points randomly in both directions, and the external magnetic field can align the magnetization directions so that the chiral current expels the magnetic field.

2.2. Paramagnetic phase

Although the existence of the paramagnetic phase in this material is not supported by the DFT calculations, we consider it in this work because the ferromagnetism and superconductivity could be competing orders, and the transition to the superconducting state could be accompanied by the disappearance of spin polarization similarly as in other systems [20–23]. In the paramagnetic phase

$$H(\boldsymbol{k}) = \begin{pmatrix} H_\uparrow(\boldsymbol{k}) & 0 \\ 0 & H_\downarrow(\boldsymbol{k}) \end{pmatrix}, \tag{13}$$

where

$$H_\uparrow(\boldsymbol{k}) = H_0(\boldsymbol{k}) + H_{\rm mb}(\boldsymbol{k}) + H_{\rm so}(\boldsymbol{k}) - \mu_{\rm P}\,\sigma_0 \tag{14}$$

and

$$H_\downarrow(\boldsymbol{k}) = H_\uparrow^T(-\boldsymbol{k})\,. \tag{15}$$

The topological properties and the energy-momentum dispersions of the bands are essentially the same as in the ferromagnetic phase because the low-energy theory consists of d_{xz} and d_{yz} orbitals, so that the atomic spin-orbit coupling does not couple the two spin blocks. Therefore, we obtain 4 similar flat bands as discussed above. The spin-Chern number $C_\uparrow(k_z)$ of the lower flat band of $H_\uparrow(\boldsymbol{k})$ as a function of k_z behaves similarly as in the ferromagnetic phase and the spin-Chern number $C_\downarrow(k_z)$ of the lower flat band of $H_\downarrow(\boldsymbol{k})$ satisfies

$$C_\downarrow(k_z) = -C_\uparrow(-k_z)\,. \tag{16}$$

However, the important difference to the ferromagnetic case is that the spin-splitting field is now absent, so that the two flat bands in each spin sector must be 3/4 filled on average in order that the total filling of the four bands is 3. This means that the Fermi level is significantly above the Weyl points [see Fig. 1 (c)] and the surface states are significantly below the Fermi level.

In addition to the symmetries discussed above, in the paramagnetic phase, the Hamiltonian (13) satisfies spinful TRS

$$s_y\sigma_0 H^T(-\boldsymbol{k})s_y\sigma_0 = H(\boldsymbol{k}) \tag{17}$$

and spin-rotation symmetry around the z-axis

$$s_z\sigma_0 H(\boldsymbol{k})s_z\sigma_0 = H(\boldsymbol{k})\,, \tag{18}$$

where we have denoted the Pauli matrices in the spin space with s_i and in the orbital space with σ_i. If $t_{z-} = 0$, the Hamiltonian also satisfies spinful mirror symmetry

$$s_x\sigma_z H(-k_x, k_y, k_z)s_x\sigma_z = H(k_x, k_y, k_z)\,. \tag{19}$$

3. Minimal models for the superconducting phase

3.1. Superconductivity in the spin-polarized phase

Since we are looking for the possibility of high-temperature superconductivity, we assume momentum-independent on-site pairing order parameter. In the spin-polarized phase the only possible order parameter, satisfying these requirements, is the interorbital order parameter which pairs the electrons in the d_{xz} and d_{yz} orbitals [50]. Therefore, we assume that the Bogoliubov–de Gennes (BdG) Hamiltonian in the spin-polarized superconducting phase is

$$H_{\mathrm{BdG}}(\boldsymbol{k}) = \begin{pmatrix} H_\uparrow(\boldsymbol{k}) & \Delta \\ \Delta^\dagger & -H_\uparrow^T(-\boldsymbol{k}) \end{pmatrix}, \tag{20}$$

where

$$\Delta = \begin{pmatrix} 0 & \Delta_0 \\ -\Delta_0 & 0 \end{pmatrix}. \tag{21}$$

Since the scale t_0 of the hopping parameters in these models is small, and we are looking for the possibility of high-temperature superconductivity, the parameter Δ_0 can be comparable to t_0.

In the absence of spin-orbit coupling ($\lambda = 0$), the Hamiltonian (20) can be written as

$$H_{\mathrm{BdG}}(\boldsymbol{k}) = H_\uparrow(\boldsymbol{k})\tau_z - \Delta_0\tau_y\sigma_y\,, \tag{22}$$

where we have denoted the Pauli matrices in the Nambu space with τ_i. This Hamiltonian satisfies a particle–hole symmetry (PHS)

$$\tau_x H_{\mathrm{BdG}}^T(-\boldsymbol{k})\tau_x = -H_{\mathrm{BdG}}(\boldsymbol{k}) \tag{23}$$

and a time-reversal symmetry

$$H_{\mathrm{BdG}}^T(-\boldsymbol{k}) = H_{\mathrm{BdG}}(\boldsymbol{k}) \tag{24}$$

so that there exists a chiral symmetry

$$\tau_x H_{\mathrm{BdG}}(\boldsymbol{k})\tau_x = -H_{\mathrm{BdG}}(\boldsymbol{k})\,. \tag{25}$$

This means that the Hamiltonian can be transformed into a block-off-diagonal form

$$U^\dagger H_{\mathrm{BdG}}(\boldsymbol{k})U = \begin{pmatrix} 0 & D(\boldsymbol{k}) \\ D^\dagger(\boldsymbol{k}) & 0 \end{pmatrix}, \tag{26}$$

where $U = (\tau_z + \tau_x)/\sqrt{2}$ and $D(\boldsymbol{k}) = H_\uparrow(\boldsymbol{k}) - \Delta$. In the presence of chiral symmetry, 3D Hamiltonians can support nodal lines, which are protected by the winding number of $z(\boldsymbol{k}) = \mathrm{Det}D(\boldsymbol{k})/|\mathrm{Det}D(\boldsymbol{k})|$ when one goes around the nodal line in the momentum space [54]. Figure 2 (a) shows that the phase diagram of the model (20) with the flat-band parameters, given in Table 1, and $t_{z-} = 0$ contains a fully gapped topologically trivial superconducting phase and two different kinds of gapless topological phases. In Type A gapless phase, the nodal lines form loops inside the Brillouin zone and in Type B gapless phase, the nodal lines go through the Brillouin zone in the k_z direction [55–57], as illustrated in Fig. 2 (b) and (c). In both cases, the nodal lines give rise to surface flat bands. The number of zero-energy surface states at the surface momentum (k_l, k_m) is determined by the winding number of $z(\boldsymbol{k})$ across the Brillouin zone in the third momentum direction k_n, as illustrated for surfaces parallel to the (y, z)-plane in Fig. 2 (d) and (e). The mirror-symmetry-breaking term H_{mb} preserves the chiral symmetry and therefore the phase diagram is qualitatively similar also when $t_{z-} \neq 0$. However, we point out that depending on the values of the model parameters, the regions of the different phases in the (μ, Δ)-plane can look very different. For example, for the H–M parameters, only the trivial phase and Type A gapless phase are present as shown in Fig. 3.

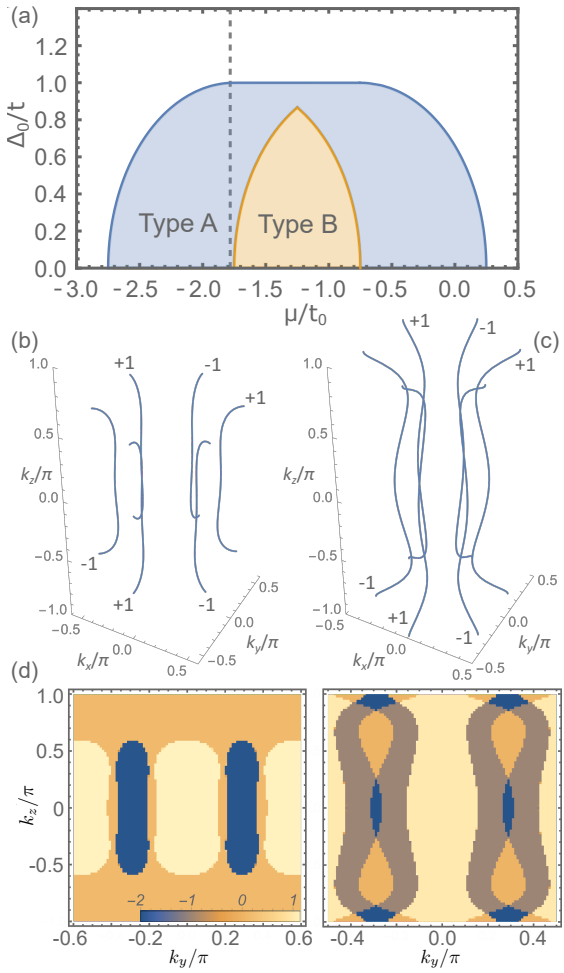

Fig. 2. (a) The phase diagram of the spin-polarized superconducting model (20) as a function of μ and Δ for $t_{z-} = \lambda = 0$ and other parameters given by the flat-band parameters in Table 1. The expected chemical potential in the ferromagnetic phase $\mu = \mu_F$ is shown with a dashed line. The phase diagram contains a topologically trivial fully gapped phase, and Type A (nodal loops) and Type B (nodal lines going through the Brillouin zone in the k_z direction) gapless topological phases. (b) The illustration of the nodal lines in the momentum space for Type A gapless phase. (c) The same for Type B gapless phase. (d) The winding number $\nu(k_y, k_z)$ determining the number of surface flat bands at the side surfaces as a function surface momentum (k_y, k_z) in Type A gapless phase. (e) The same for Type B gapless phase. In (b) and (d), the parameters are $\mu = -1.7$ and $\Delta = 0.8$. In (c) and (e), the parameters are $\mu = -1.7$ and $\Delta = 0.3$.

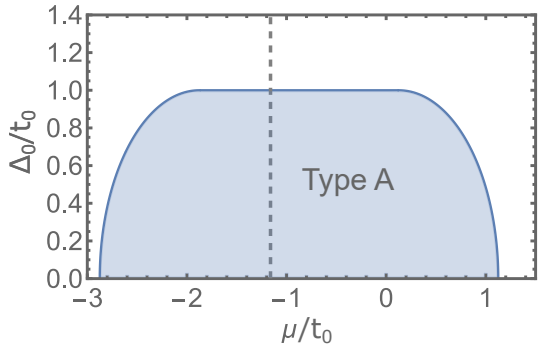

Fig. 3. The phase diagram of the spin-polarized superconducting model (20) as a function of μ and Δ for $t_{z-} = \lambda = 0$ and other parameters given by the H–M parameters in Table 1. The expected chemical potential in the ferromagnetic phase $\mu = \mu_F$ is shown with a dashed line. In this case the phase diagram contains only the trivial phase and Type A gapless phase.

The presence of spin-orbit coupling ($\lambda \neq 0$) breaks the chiral symmetry. Nevertheless, it follows from the symmetries discussed in Section 2 and from the fact that spin-orbit coupling (9) is momentum-independent that

$$H_{\mathrm{BdG}}(0, -k_y, k_z) = H_{\mathrm{BdG}}(0, k_y, k_z)\,. \tag{27}$$

Together with the PHS (23), this guarantees that there exists a $\mathbb{Z}_2$-Pfaffian invariant [58, 59], which can give rise to topologically protected band crossings in the plane $k_x = 0$ (and in the other planes related to this by the three-fold rotational symmetry). We indeed find that this kind of topological nodal lines exist in a large part of the parameter space as shown in Fig. 4 (a). When both spin-orbit coupling ($\lambda \neq 0$) and mirror-symmetry breaking ($t_{z-} \neq 0$) are present, the symmetry (27) exists only in the planes $k_z = 0,\ \pi$. Therefore, it no longer protects nodal lines but instead, we obtain the topologically protected Majorana–Weyl points at the high-symmetry lines as shown in Fig. 4 (b). Even in the absence of the Weyl points, the model can support topologically distinct phases because the Chern number calculated for the two lowest bands of the BdG Hamiltonian (20) in the $k_z = 0$ plane can have values -2 or 0 as shown in Fig. 4.

We point out that in Fig. 4, we have only characterized the phases in terms of the topologically protected band crossings at the high-symmetry planes and lines discussed above, but there can also be gap closings in other parts of the Brillouin zone. In particular, the phases are expected to be gapless in some regions of the parameter space because the breaking of the chiral symmetry enables the possibility of indirect gap closings.

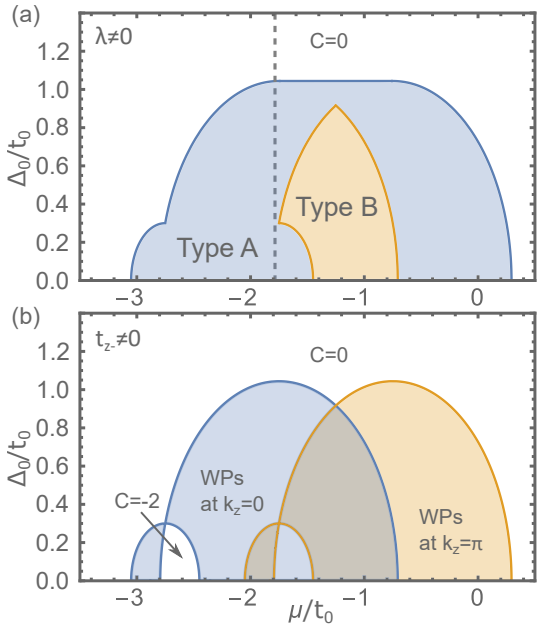

Fig. 4. The phase diagrams of the spin-polarized superconducting model (20) as a function of μ and Δ for the flat-band parameters given in Table 1 in the presence of symmetry-breaking terms. (a) In the presence of spin-orbit coupling $\lambda = 0.3t_0$, the phase diagrams contain Type A and Type B gapless phases protected by the combination of the symmetries (23) and (27). (b) In the presence of spin-orbit coupling $\lambda = 0.3t_0$ and mirror-symmetry breaking $t_{z-} = t_0/12$, the symmetry (27) is valid only at $k_z = 0,\ \pi$. The protected Weyl points (WPs) at these planes are shown with blue and orange colors. The $C = -2$ indicates a region, where the two lowest bands of the BdG Hamiltonian (20) carry a Chern number $C = -2$ at the $k_z = 0$ plane. Therefore, it is topologically distinct from the trivial $C = 0$ phase.

3.2. Superconductivity in the paramagnetic phase

In the case of paramagnetic phase, the most likely candidate for the momentum-independent order parameter is the s-wave singlet pairing. Therefore, the BdG Hamiltonian in this case is

$$H_{\mathrm{BdG}}(\boldsymbol{k}) = \begin{pmatrix} H_{\uparrow}(\boldsymbol{k}) & \Delta_0\sigma_0 \\ \Delta_0\sigma_0 & -H_{\downarrow}^{T}(-\boldsymbol{k}) \end{pmatrix}. \tag{28}$$

Due to the spinful TRS $H_{\downarrow}^{T}(-\boldsymbol{k}) = H_{\uparrow}(\boldsymbol{k})$, this Hamiltonian satisfies a chiral symmetry

$$\tau_y H_{\mathrm{BdG}}(\boldsymbol{k})\tau_y = -H_{\mathrm{BdG}}(\boldsymbol{k})\,. \tag{29}$$

For $\Delta_0 \neq 0$, this Hamiltonian is always fully gapped and topologically trivial.

4. Superfluid weight

Using linear-response theory, the in-plane supercurrent response to the gradient of the phase can be expressed as

$$j_i = \frac{g_s}{2}\frac{\hbar}{2e}[D_s]_{ij}\left(\partial_j\phi - \frac{2e}{\hbar}A_j\right), \tag{30}$$

where due to the three-fold rotational symmetry $[D_s]_{xy} = [D_s]_{yx} = 0$, $[D_s]_{xx} = [D_s]_{yy} = D_s$, and

$$D_s = \frac{e^2}{\hbar^2}\frac{1}{V}\sum_{\boldsymbol{k},i,j}\frac{n_F(E_j(\boldsymbol{k})) - n_F(E_i(\boldsymbol{k}))}{E_i(\boldsymbol{k}) - E_j(\boldsymbol{k})}$$
$$\times\left\{\left|\langle\psi_i(\boldsymbol{k})|\frac{\partial H_{\mathrm{BdG}}(\boldsymbol{k})}{\partial k_x}|\psi_j(\boldsymbol{k})\rangle\right|^2 - \left|\langle\psi_i(\boldsymbol{k})|\frac{\partial H_{\mathrm{BdG}}(\boldsymbol{k})}{\partial k_x}\tau_z|\psi_j(\boldsymbol{k})\rangle\right|^2\right\}. \tag{31}$$

Here, the degeneracy factor $g_s = 1$ in the spin-polarized model (20) and $g_s = 2$ in the case of the time-reversal invariant singlet superconducting model (28), V is the volume of the sample, and $|\psi_i(\boldsymbol{k})\rangle$ and $E_i(\boldsymbol{k})$ are the eigenstates and eigenenergies of $H_{\mathrm{BdG}}(\boldsymbol{k})$, respectively. In the derivation of Eq. (31), we also utilized the momentum independence of the superconducting order parameter. In our numerical results, we express the superfluid weight in units $D_0 = e^2 t_0/\hbar^2$. This is the natural choice of unit, because in these units, the conventional contribution to the superfluid weight, $D_{s,\mathrm{conv}} \approx e^2 n/m^*$, in the middle of the upper weakly dispersive band in the singlet superconducting phase is expected to be of the order $D_{s,\mathrm{conv}}/D_0 \sim 1$. All the shown results are calculated at zero temperature.

It is useful to decompose D_s to the conventional contribution determined by the single-particle spectrum (analogous to the conventional single-band case discussed above) and the contribution determined by the quantum geometry of the bands (interband contributions) [22, 40–46]. For this purpose, we express the superfluid weight in terms of the eigenstates of the normal-state Bloch Hamiltonian $H_{\mathrm{BdG}}(\boldsymbol{k}, \Delta = 0)$. In the spin-polarized case (20), we decompose the BdG eigenstates as

$$|\psi_i\rangle = \sum_{m=1}^{N}\left[w_{+,im}\begin{pmatrix}|m(\boldsymbol{k})\rangle\\ 0\end{pmatrix} + w_{-,im}\begin{pmatrix}0\\ |m(-\boldsymbol{k})\rangle^*\end{pmatrix}\right], \tag{32}$$

where $|m(\boldsymbol{k})\rangle$ is the eigenvector of $H_\uparrow(\boldsymbol{k})$ with eigenvalue $\varepsilon_m(\boldsymbol{k})$ and $|m(-\boldsymbol{k})\rangle^*$ is the eigenvector of $H_\uparrow^T(-\boldsymbol{k})$ with eigenvalue $\varepsilon_m(-\boldsymbol{k})$. In the case of the time-reversal invariant singlet superconductor (28), we perform the same expansion except that we replace $|m(-\boldsymbol{k})\rangle^*$ with the eigenvectors $|m(\boldsymbol{k})\rangle$ of

$H_{\downarrow}^{T}(-\boldsymbol{k}) = H_{\uparrow}(\boldsymbol{k})$ with eigenvalue $\varepsilon_m(\boldsymbol{k})$. By inserting this decomposition into Eq. (31) and keeping only the intraband contributions, we obtain the following expression for the conventional part of the superfluid weight:

$$D_{s,\mathrm{conv}} = -\frac{e^2}{\hbar^2}\frac{4}{V}\sum_{\boldsymbol{k},ijmn}\frac{n(E_j(\boldsymbol{k}))-n(E_i(\boldsymbol{k}))}{E_i(\boldsymbol{k})-E_j(\boldsymbol{k})}w^*_{+,im}w_{+,jm}w^*_{-,jn}w_{-,in}M_{mn}(\boldsymbol{k})\,, \tag{33}$$

where in the spin-polarized case (20)

$$M_{mn}(\boldsymbol{k}) = \partial_{k_x}\varepsilon_m(\boldsymbol{k})\partial_{k_x}\varepsilon_n(-\boldsymbol{k})\,, \tag{34}$$

and in the singlet superconducting case (28)

$$M_{mn}(\boldsymbol{k}) = \partial_{k_x}\varepsilon_m(\boldsymbol{k})\partial_{k_x}\varepsilon_n(\boldsymbol{k})\,. \tag{35}$$

The geometric contribution is obtained as

$$D_{s,\mathrm{geom}} = D_s - D_{s,\mathrm{conv}}\,. \tag{36}$$

The standard paradigm of flat-band superconductivity is the time-reversal invariant s-wave singlet superconductivity in a system with spin-rotation symmetry around the z-axis supporting a well-isolated flat band [40, 41]. In this case, $D_{s,\mathrm{conv}} = 0$ and

$$D_{s,\mathrm{geom}} = \frac{8e^2}{\hbar^2}\Delta_0\sqrt{\nu(1-\nu)}\int\frac{\mathrm{d}^d k}{(2\pi)^d}\,g_{xx}(\boldsymbol{k})\,, \tag{37}$$

where ν is the band filling and d is the dimension of the system. The quantum metric $g_{\mu\nu}(\boldsymbol{k})$ is given by the real part of the quantum geometric tensor

$$\mathcal{B}_{\mu\nu}(\boldsymbol{k}) = \langle\partial_{k_\mu}n(\boldsymbol{k})|\,(1-|n(\boldsymbol{k})\rangle\langle n(\boldsymbol{k})|)\,\partial_{k_\nu}n(\boldsymbol{k})\rangle\,, \tag{38}$$

where $|n(\boldsymbol{k})\rangle$ is the normal-state Bloch wave function of the flat band. The imaginary part of $\mathcal{B}_{xy}(\boldsymbol{k})$ is $\Omega(\boldsymbol{k})/2$, where $\Omega(\boldsymbol{k})$ is the Berry curvature. Since $\mathcal{B}_{\mu\nu}(\boldsymbol{k})$ is positive semidefinite, in a two-dimensional system (or in a plane with fixed k_z in a three-dimensional system)

$$\int\mathrm{d}^2k\,g_{xx}(\boldsymbol{k}) = \int\mathrm{d}^2k\,g_{yy}(\boldsymbol{k}) \geq \frac{1}{2}\int\mathrm{d}^2k\,|\Omega(\boldsymbol{k})| \geq \pi|C|\,, \tag{39}$$

where $C = \frac{1}{2\pi}\int\mathrm{d}^2k\,\Omega(\boldsymbol{k})$ is the Chern number. This means that if this type of system supports spin-up and spin-down flat bands carrying opposite spin-Chern numbers, there exists a lower bound for D_s determined by the absolute value of the Chern number [40].

As discussed in Section 2, the normal-state Hamiltonians considered in this paper support nontrivial Chern numbers for large ranges of k_z values. Therefore, one might be tempted to conclude that the superfluid weight has a lower bound in these systems. This conclusion is, however, wrong, because the models do not satisfy the assumptions required for the existence of the universal lower bounds. In the case of spin-polarized superconductivity (20), the assumptions about singlet superconductivity and time-reversal symmetry are not satisfied. Additionally, in both models (20) and (28), the bands are not well-isolated and they are not perfectly flat. In the following, we discuss how these deviations from the idealized model influence the superfluid weight. In order to better understand our results, we write the Hamiltonian $H_\uparrow(\boldsymbol{k})$ as

$$H_\uparrow(\boldsymbol{k}) = \sum_{\mu=0}^{4} d_\mu^\uparrow(\boldsymbol{k})\sigma_\mu \,, \tag{40}$$

where $d_0^\uparrow(\boldsymbol{k}) = d_0(\boldsymbol{k}) - \mu$, $d_1^\uparrow(\boldsymbol{k}) = d_1(\boldsymbol{k})$, $d_2^\uparrow(\boldsymbol{k}) = d_2(\boldsymbol{k}) - 2t_{z-}\sin k_z + \lambda$, $d_3^\uparrow(\boldsymbol{k}) = d_3(\boldsymbol{k})$, and $d_\mu(\boldsymbol{k})$ are given in Eq. (1). Then we introduce a perturbation to our Hamiltonian

$$\tilde{H}_\uparrow(\boldsymbol{k}) = \xi \begin{pmatrix} \frac{|d^\uparrow(\boldsymbol{k})| - d_z^\uparrow(\boldsymbol{k})}{2|d^\uparrow(\boldsymbol{k})|} & -\frac{d_x^\uparrow(\boldsymbol{k}) - id_y^\uparrow(\boldsymbol{k})}{2|d^\uparrow(\boldsymbol{k})|} \\ -\frac{d_x^\uparrow(\boldsymbol{k}) + id_y^\uparrow(\boldsymbol{k})}{2|d^\uparrow(\boldsymbol{k})|} & \frac{|d^\uparrow(\boldsymbol{k})| + d_z^\uparrow(\boldsymbol{k})}{2|d^\uparrow(\boldsymbol{k})|} \end{pmatrix} , \tag{41}$$

where $|d^\uparrow(\boldsymbol{k})|^2 = d_x^\uparrow(\boldsymbol{k})^2 + d_y^\uparrow(\boldsymbol{k})^2 + d_z^\uparrow(\boldsymbol{k})^2$. This perturbation does not modify the eigenstates $|n(\boldsymbol{k})\rangle$ of the normal-state Hamiltonian but shifts the lower band in energy by a constant ξ. Therefore, by controlling the magnitude of ξ in this perturbation, we can tune our model from the ideal case of an isolated flat band to the actual models proposed for the copper-doped lead apatite.

4.1. Superfluid weight in the superconducting spin-polarized phase

Although the normal-state bands support nontrivial topology and quantum geometry, we find that in the spin-polarized case, there is no lower bound for D_s. As shown in Fig. 5 (a), the superfluid weight can be even negative for a wide range of μ and Δ_0 values, indicating instability of the spatially homogeneous superconducting state. In general, we find that D_s varies a lot depending on the values of the model parameters. For the H–M parameters, we obtain much larger values of D_s, $D_{s,\mathrm{geom}}$, and $D_{s,\mathrm{conv}}$ than for the flat-band parameters as shown in Fig. 5 (a) and (b) and Fig. 6. On the other hand, realistic values of mirror-symmetry-breaking hopping ($t_z = t_0/12$) and spin-orbit coupling ($\lambda = 0.3t_0$) do not increase D_s significantly [see Fig. 6 (a)]

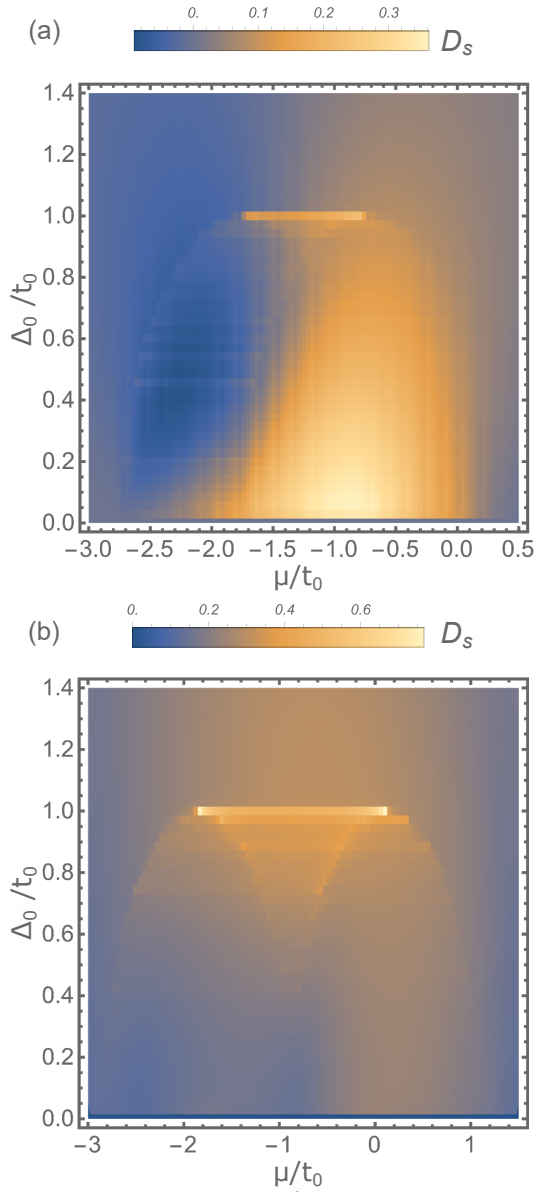

Fig. 5. (a) Superfluid weight as a function of μ and Δ_0 for the superconducting model (20) with $t_{z-} = \lambda = 0$ and other parameters given by the flat-band parameters in Table 1. (b) The same for the H–M parameters in Table 1.

even though they have significant effects on the topologies of the normal and superconducting states. This demonstrates that the nontrivial topology of the bands does not improve the superconductivity in the spin-polarized case.

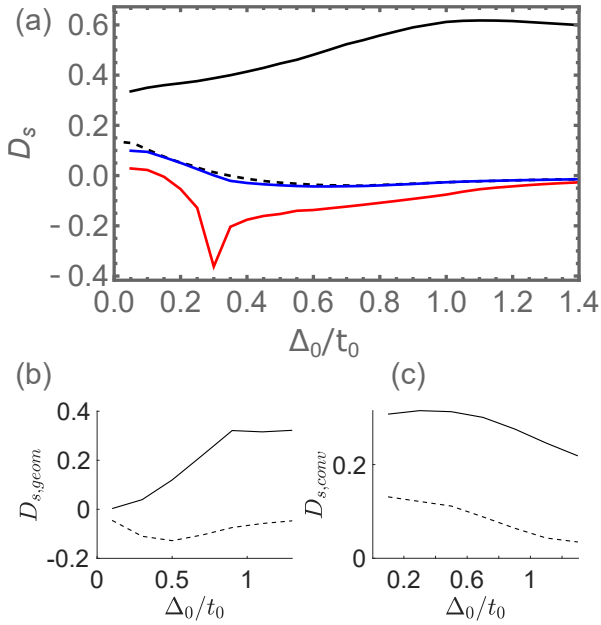

Fig. 6. (a) Superfluid weight D_s as a function of Δ_0 for $\mu = \mu_{\mathrm{F}}$. The black (dashed) line shows D_s for the H–M (flat-band parameters) in Table 1. The blue (red) line shows the effect of mirror-symmetry-breaking hopping $t_{z-} = t_0/12$ (spin-orbit coupling $\lambda = 0.3t_0$) when the other parameters are given by the flat-band parameters. (b) and (c) $D_{s,\mathrm{geom}}$ and $D_{s,\mathrm{conv}}$ as a function of Δ_0 for the H–M (solid line) and flat-band (dashed line) parameters in Table 1.

4.2. Superfluid weight in the nonuniform superconducting spin-polarized phase

To uncover the meaning of the negative D_s shown in Fig. 5 (a), we focus on a simplified system with the flat-band parameters and uncoupled layers $t_z = 0$, and optimize the phase of the superconducting order parameter in the real space. To accomplish this, we choose $\mu = -2.133t_0$ and $\Delta_0 = 0.308t_0$ from the region of the (μ, Δ_0)-plane, where $D_s < 0$ in the case of homogeneous superconducting state. In this case, the homogeneous superconducting state should be unstable, so we consider a three times larger unit cell in both directions and optimize the phases of local $\Delta_{i,j}$, with $i, j \in \{1, 2, 3\}$, using the classical Monte Carlo algorithm. In this way, we find that the lowest-energy state at this particular (μ, Δ_0) point is not the one with uniform phase, see Fig. 7 (a), but rather the one shown in Fig. 7 (b), where $\arg(\Delta_{i,j})$ changes by 120° with every lattice translation. This may also be considered as a vortex state where each unit cell has one

double vortex-double antivortex pair. The energy difference $E_{\mathrm{uni}} - E_{120}$ between the uniform and nonuniform 120° spin-polarized superconducting states is shown in Fig. 8 demonstrating that the transition between these phases occurs approximately at $\mu \approx -1.4t_0$ for every Δ_0.

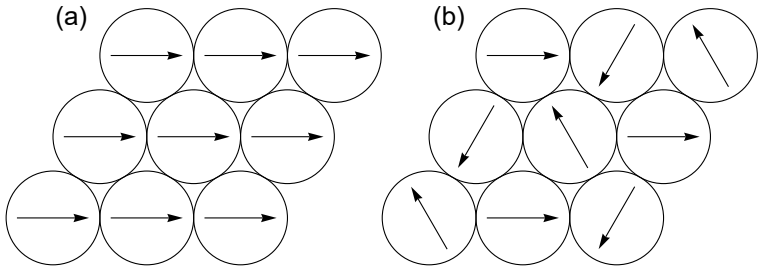

Fig. 7. Schematic view of (a) uniform and (b) nonuniform 120° spin-polarized superconducting phase. Circles symbolize sites of the triangular lattice and arrow $\arg(\Delta_{i,j})$. The unit cell contains 3 lattice sites in each direction.

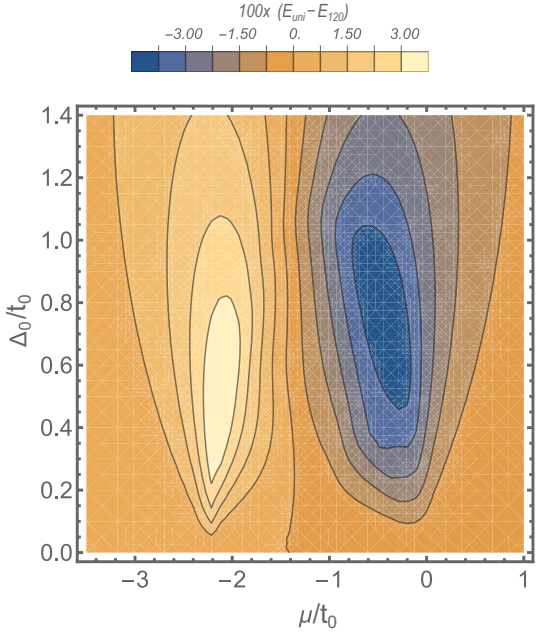

Fig. 8. Energy difference $E_{\mathrm{uni}} - E_{120}$ between the uniform and nonuniform 120° spin-polarized states as a function of μ and Δ_0 for the flat-band parameters with uncoupled layers $t_z = 0$.

The superfluid weights D_s for both phases are shown in Fig. 9 (a) and (b). Around $\mu = -2.133t_0$ and $\Delta_0 = 0.308t_0$, D_s is negative in the uniform state and positive for the nonuniform 120° state indicating that the configuration of the phases found by the Monte Carlo algorithm is indeed stable in this

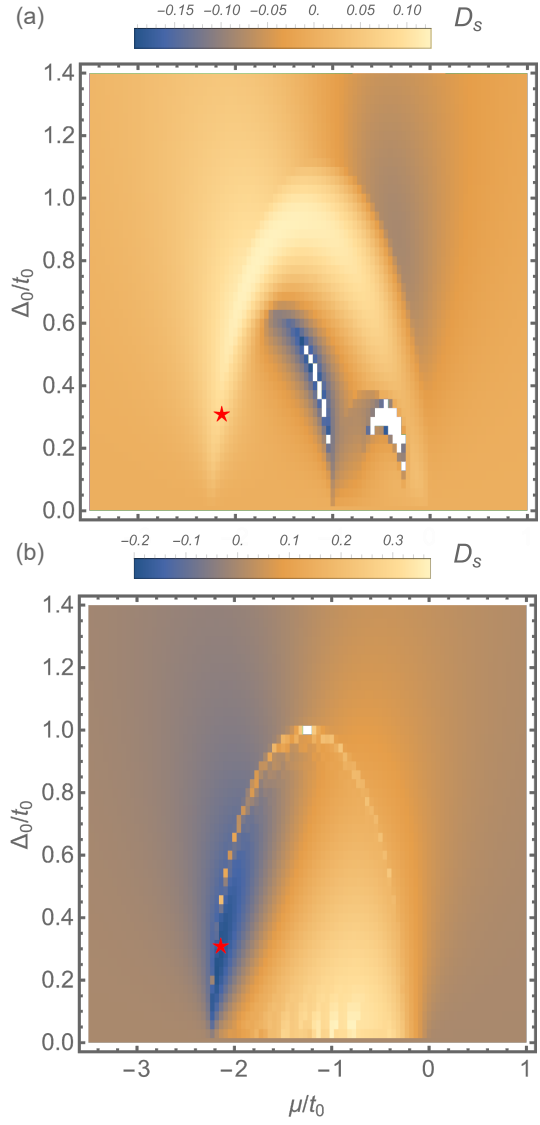

Fig. 9. D_s as a function of μ and Δ_0 for (a) nonuniform 120° and (b) uniform spin-polarized superconducting states with flat-band parameters and uncoupled layers $t_z = 0$. The red star marks the point at which the nonuniform 120° state was obtained as the lowest-energy configuration.

region of the parameter space. Figure 10 shows D_s when we have chosen for each μ and Δ_0 either the uniform or nonuniform 120° spin-polarized superconducting state depending on which one has lower energy, *cf.* Fig. 8. We notice that D_s is now positive almost everywhere in the (μ, Δ_0)-plane but small regions of negative D_s remain near the transition line between the phases. This indicates that close to the transition line, the lowest-energy configuration is given by an even more complicated pattern of $\arg(\Delta_{i,j})$.

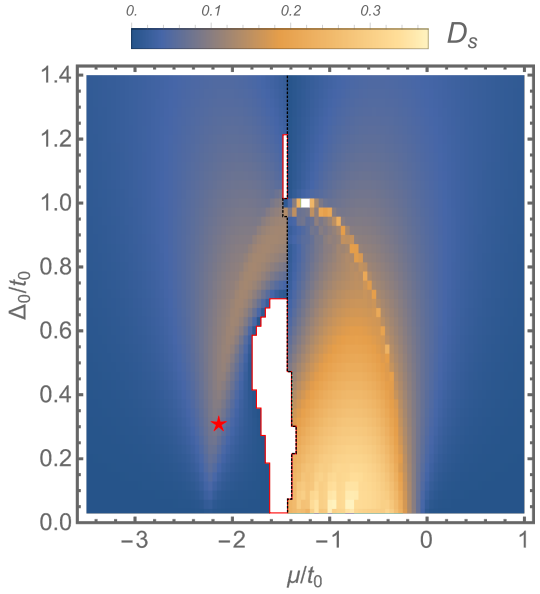

Fig. 10. D_s as a function of μ and Δ_0 for the flat-band parameters and uncoupled layers $t_z = 0$ with the spin-polarized superconducting state being either nonuniform 120° or uniform state, depending on which one has lower energy. The black dashed line marks the boundary between the uniform and non-uniform phases. In white regions framed in red appearing close to the transition line, we find $D_s < 0$, indicating that in these regions, the lowest-energy configuration is given by an even more complicated pattern of $\arg(\Delta_{i,j})$.

4.3. Superfluid weight in the time-reversal invariant singlet s-wave superconducting phase

In the case of time-reversal invariant s-wave singlet superconducting phase (28), the system obeys the spin-rotation symmetry around the z-axis. Therefore, the corrections to the result (37) only come from the facts that the bands are not well-isolated and they are not perfectly flat. We find that in this case, the superfluid weight is large for all reasonable values of μ and

Δ_0 [Fig. 11 (a)], and it contains a significant geometric component in the case of strong coupling superconductivity $\Delta_0 > 0.7t_0$ [Fig. 11 (b)]. The increase in the bandwidth caused by the H–M parameters relative to the flat-band parameters [see Fig. 1 (b)] increases the superfluid weight [see Fig. 11 (c)] because the conventional contribution is increased. The mirror-symmetry-breaking hopping ($t_z = t_0/12$) and spin-orbit coupling ($\lambda = 0.3t_0$) do not significantly affect the results for D_s as shown in Fig. 11 (c).

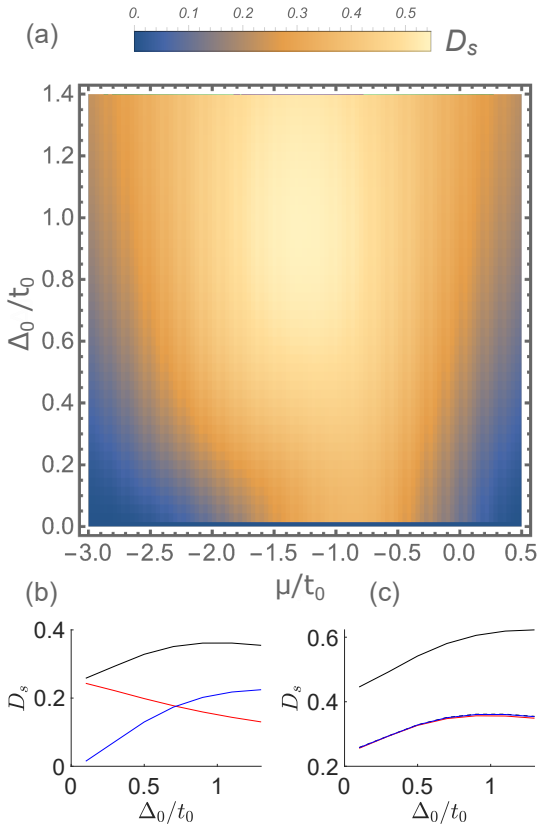

Fig. 11. (a) Superfluid weight as a function of μ and Δ_0 for the superconducting model (28) with $t_{z-} = \lambda = 0$ and other parameters given by the flat-band parameters in Table 1. (b) D_s (black), $D_{s,\mathrm{conv}}$ (red), and $D_{s,\mathrm{geom}}$ (blue) as a function of Δ_0 for $\mu = \mu_{\mathrm{P}}$ and otherwise the same parameters. (c) The spin-orbit coupling $\lambda = 0.3t_0$ (red line) and the mirror-symmetry-breaking hopping $t_{z-} = t_0/12$, (blue line) do not influence the results significantly. The superfluid weight with flat-band parameters and $\lambda = t_{z-} = 0$ is shown with a dashed line as a reference. On the other hand, D_s is larger for the H–M parameters in Table 1 (solid black line).

In the case of singlet superconductivity, D_s is fully determined by the quantum geometry (37) in the limit where we have an isolated ($\xi = -100t_0$) perfectly flat band ($t_z = 0$) obtained with the help of the perturbation (41) as shown in Fig. 12 (a). When ξ is decreased so that the bands are coupled, the total superfluid weight D_s slightly decreases in magnitude. The decrease of the geometric contribution $D_{s,\mathrm{geom}}$ [Fig. 12 (b)] is partially compensated by the increase of the conventional contribution $D_{s,\mathrm{conv}}$ [Fig. 12 (c)]. We point out that the integral of the quantum metric

$$G = \frac{1}{(2\pi)^3} \int \mathrm{d}^3k \, g_{xx}(\boldsymbol{k}) \tag{42}$$

can be very large in our model. In fact, it diverges logarithmically as $\lambda \to 0$ [see Fig. 12 (d)]

$$G \approx 0.11 + \frac{1}{8\pi} \ln(1/\lambda) \,, \tag{43}$$

because the energy bands become degenerate along the Γ–A line. This divergence of G does not, however, show up in the superfluid weight D_s

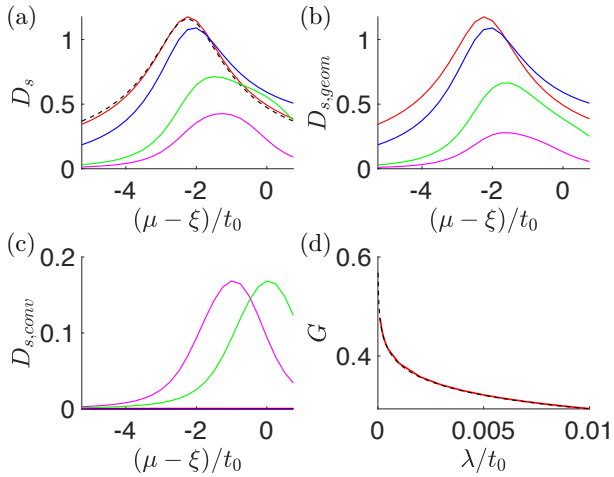

Fig. 12. (a) D_s as a function of μ for the superconducting model (28) with $t_z = t_{z-} = 0$, $\lambda = 0.01t_0$, $\Delta_0 = t_0$, and other hopping parameters given by the flat-band parameters in Table 1. Additionally, we have introduced the perturbation (41), which shifts the lower band by an energy $\xi = 0$ (magenta), $\xi = -t_0$ (green), $\xi = -10t_0$ (blue), and $\xi = -100t_0$ (red) without modifying the eigenstates. The dashed black line shows the analytic results (37). (b), (c) The same for $D_{s,\mathrm{geom}}$ and $D_{s,\mathrm{conv}}$, respectively. $D_{s,\mathrm{conv}} \approx 0$ for all values of μ when $\xi/t_0 =: -100, -10$. (d) Integral of the quantum metric G [Eq. (42)] as a function of λ (red line). The dashed black line shows the asymptotic behavior of G [Eq. (43)] when approaching the degeneracy of the bands ($\lambda \to 0$).

because the coupling of the bands becomes more and more important when approaching the degeneracy.

5. Discussion and conclusions

We have computed the geometric and conventional contributions of the superfluid weight for the superconducting flat-band models proposed for the doped lead apatite. We have found that, in contrast to the standard paradigms of flat-band superconductivity, there does not exist any lower bound for the superfluid weight in these models. Moreover, although the nontrivial quantum geometries of the normal-state bands are the same in the ferromagnetic and paramagnetic phases, the emerging superconducting phases have very different superfluid weights. Namely, we find that the ferromagnetic phase found in the DFT calculations could, in principle, support a variety of topologically nontrivial spin-polarized superconducting phases, but our results for the superfluid weight show that their capabilities to support supercurrents can vary a lot depending on the values of the model parameters. In particular, there can even exist parameter regions where the homogeneous superconducting state becomes unstable. On the other hand, if the transition to the superconducting state is accompanied by the disappearance of spin polarization, the superfluid weight in the time-reversal invariant singlet superconducting state is robustly large and it contains a significant quantum geometric component. We have also shown that the spin-orbit coupling and mirror-symmetry-breaking terms in the Hamiltonian do not significantly affect the results for the superfluid weight even though they influence the normal-state topology of the flat bands.

W.B. acknowledges support by the National Science Centre (NCN), Poland, projects No. 2019/34/E/ST3/00404 and 2021/43/B/ST3/02166.

REFERENCES

[1] S. Lee, J.-H. Kim, Y.-W. Kwon, «The First Room-Temperature Ambient-Pressure Superconductor», arXiv:2307.12008 [cond-mat.supr-con].

[2] S. Lee *et al.*, «Superconductor $Pb_{10-x}Cu_x(PO_4)_6O$ showing levitation at room temperature and atmospheric pressure and mechanism», arXiv:2307.12037 [cond-mat.supr-con].

[3] H. Wu, L. Yang, B. Xiao, H. Chang, «Successful growth and room temperature ambient-pressure magnetic levitation of LK-99», arXiv:2308.01516 [cond-mat.supr-con].

[4] Q. Hou *et al.*, «Synthesis, transport and magnetic properties of Cu-doped apatite in $Pb_{10-x}Cu_x(PO_4)_6O$», *Matter* **6**, 4408 (2023), arXiv:2308.01192 [cond-mat.supr-con].

[5] K. Guo, Y. Li, S. Jia, «Ferromagnetic half levitation of LK-99-like synthetic samples», *Sci. China Phys. Mech. Astron.* **66**, 107411 (2023).

[6] K. Kumar, N. Kumar Karn, Y. Kumar, V. Awana, «Absence of Superconductivity in LK-99 at Ambient Conditions», *ACS Omega* **8**, 41737 (2023).

[7] P.K. Jain, «Superionic Phase Transition of Copper(I) Sulfide and Its Implication for Purported Superconductivity of LK-99», *J. Phys. Chem. C* **127**, 18253 (2023).

[8] S. Zhu, W. Wu, Z. Li, J. Luo, «First-order transition in LK-99 containing Cu_2S», *Matter* **6**, 4401 (2023).

[9] H. Wang *et al.*, «Indications of superconductivities in blend of variant apatite and covellite», arXiv:2406.17525 [cond-mat.supr-con].

[10] H. Wang *et al.*, «Observation of diamagnetic strange-metal phase in sulfur–copper codoped lead apatite», arXiv:2403.11126 [cond-mat.supr-con].

[11] H. Wang *et al.*, «Possible Meissner effect near room temperature in copper-substituted lead apatite», arXiv:2401.00999 [cond-mat.supr-con].

[12] S.M. Griffin, «Origin of correlated isolated flat bands in copper-substituted lead phosphate apatite», arXiv:2307.16892 [cond-mat.supr-con].

[13] L. Si, K. Held, «Electronic structure of the putative room-temperature superconductor $Pb_9Cu(PO_4)_6O$», *Phys. Rev. B* **108**, L121110 (2023), arXiv:2308.00676 [cond-mat.supr-con].

[14] R. Kurleto *et al.*, «Pb-apatite framework as a generator of novel flat-band CuO based physics, including possible room temperature superconductivity», arXiv:2308.00698 [cond-mat.supr-con].

[15] J. Cabezas-Escares *et al.*, «Electronic structure and vibrational stability of copper-substituted lead apatite LK-99», *Phys. Rev. B* **109**, 144515 (2024), arXiv:2308.01135 [cond-mat.supr-con].

[16] Y. Jiang *et al.*, «$Pb_9Cu(PO4)_6(OH)_2$: Phonon bands, localized flat band magnetism, models, and chemical analysis», *Phys. Rev. B* **108**, 235127 (2023), arXiv:2308.05143 [cond-mat.supr-con].

[17] N.B. Kopnin, T.T. Heikkilä, G.E. Volovik, «High-temperature surface superconductivity in topological flat-band systems», *Phys. Rev. B* **83**, 220503 (2011).

[18] K. Moon *et al.*, «Spontaneous interlayer coherence in double-layer quantum Hall systems: Charged vortices and Kosterlitz–Thouless phase transitions», *Phys. Rev. B* **51**, 5138 (1995).

[19] J.K. Jain, «Composite Fermions», *Cambridge University Press*, Cambridge 2007.

[20] T. Löthman, A.M. Black-Schaffer, «Universal phase diagrams with superconducting domes for electronic flat bands», *Phys. Rev. B* **96**, 064505 (2017).

[21] R. Ojajärvi, T. Hyart, M.A. Silaev, T.T. Heikkilä, «Competition of electron–phonon mediated superconductivity and Stoner magnetism on a flat band», *Phys. Rev. B* **98**, 054515 (2018).

[22] X. Hu, T. Hyart, D.I. Pikulin, E. Rossi, «Quantum-metric-enabled exciton condensate in double twisted bilayer graphene», *Phys. Rev. B* **105**, L140506 (2022), arXiv:2008.03241 [cond-mat.mes-hall].

[23] A. Lau *et al.*, «Designing Three-Dimensional Flat Bands in Nodal-Line Semimetals», *Phys. Rev. X* **11**, 031017 (2021).

[24] Y. Cao *et al.*, «Unconventional superconductivity in magic-angle graphene superlattices», *Nature* **556**, 43 (2018).

[25] Y. Cao *et al.*, «Correlated insulator behaviour at half-filling in magic-angle graphene superlattices», *Nature* **556**, 80 (2018).

[26] M. Yankowitz *et al.*, «Tuning superconductivity in twisted bilayer graphene», *Science* **363**, 1059 (2019).

[27] X. Lu *et al.*, «Superconductors, orbital magnets and correlated states in magic-angle bilayer graphene», *Nature* **574**, 653 (2019).

[28] P. Stepanov *et al.*, «Untying the insulating and superconducting orders in magic-angle graphene», *Nature* **583**, 375 (2020).

[29] Y. Saito *et al.*, «Independent superconductors and correlated insulators in twisted bilayer graphene», *Nat. Phys.* **16**, 926 (2020).

[30] M. Serlin *et al.*, «Intrinsic quantized anomalous Hall effect in a moiré heterostructure», *Science* **367**, 900 (2020).

[31] G. Chen *et al.*, «Tunable correlated Chern insulator and ferromagnetism in a moiré superlattice», *Nature* **579**, 56 (2020).

[32] J.M. Park *et al.*, «Tunable strongly coupled superconductivity in magic-angle twisted trilayer graphene», *Nature* **590**, 249 (2021).

[33] Z. Hao *et al.*, «Electric field–tunable superconductivity in alternating-twist magic-angle trilayer graphene», *Science* **371**, 1133 (2021).

[34] Y. Cao *et al.*, «Pauli-limit violation and re-entrant superconductivity in moiré graphene», *Nature* **595**, 526 (2021).

[35] H. Zhou *et al.*, «Superconductivity in rhombohedral trilayer graphene», *Nature* **598**, 434 (2021).

[36] H. Zhou *et al.*, «Isospin magnetism and spin-polarized superconductivity in Bernal bilayer graphene», *Science* **375**, 774 (2022).

[37] S.-W. Kim, K. Haule, G.L. Pascut, B. Monserrat, «Non-Fermi liquid to charge-transfer Mott insulator in flat bands of copper-doped lead apatite», *Mater. Horiz.* **11**, 5622 (2024).

[38] D.J. Scalapino, S.R. White, S.C. Zhang, «Superfluid density and the Drude weight of the Hubbard model», *Phys. Rev. Lett.* **68**, 2830 (1992).

[39] D.J. Scalapino, S.R. White, S. Zhang, «Insulator, metal, or superconductor: The criteria», *Phys. Rev. B* **47**, 7995 (1993).

[40] S. Peotta, P. Törmä, «Superfluidity in topologically nontrivial flat bands», *Nat. Commun.* **6**, 8944 (2015).

[41] L. Liang *et al.*, «Band geometry, Berry curvature, and superfluid weight», *Phys. Rev. B* **95**, 024515 (2017).

[42] X. Hu, T. Hyart, D.I. Pikulin, E. Rossi, «Geometric and Conventional Contribution to the Superfluid Weight in Twisted Bilayer Graphene», *Phys. Rev. Lett.* **123**, 237002 (2019).

[43] F. Xie, Z. Song, B. Lian, B.A. Bernevig, «Topology-Bounded Superfluid Weight in Twisted Bilayer Graphene», *Phys. Rev. Lett.* **124**, 167002 (2020).

[44] A. Julku *et al.*, «Superfluid weight and Berezinskii–Kosterlitz–Thouless transition temperature of twisted bilayer graphene», *Phys. Rev. B* **101**, 060505 (2020).

[45] E. Rossi, «Quantum metric and correlated states in two-dimensional systems», *Curr. Opin. Solid State Mater. Sci.* **25**, 100952 (2021).

[46] P. Törmä, S. Peotta, B.A. Bernevig, «Superconductivity, superfluidity and quantum geometry in twisted multilayer systems», *Nat. Rev. Phys.* **4**, 528 (2022).

[47] A. Lau *et al.*, «Universal suppression of superfluid weight by non-magnetic disorder in *s*-wave superconductors independent of quantum geometry and band dispersion», *SciPost Phys.* **13**, 086 (2022).

[48] M.M. Hirschmann, J. Mitscherling, «Symmetry-enforced double Weyl points, multiband quantum geometry, and singular flat bands of doping-induced states at the Fermi level», *Phys. Rev. Mater.* **8**, 014201 (2024), arXiv:2308.03751 [cond-mat.mes-hall].

[49] P.A. Lee, Z. Dai, «Effective model for $Pb_9Cu(PO_4)_6O$», arXiv:2308.04480 [cond-mat.supr-con].

[50] O. Tavakol, T. Scaffidi, «Minimal model for the flat bands in copper-substituted lead phosphate apatite: Strong diamagnetism from multiorbital physics», *Phys. Rev. B* **109**, L100504 (2024), arXiv:2308.01315 [cond-mat.supr-con].

[51] B.T. Zhou, M. Franz, «Cu-substituted lead phosphate apatite as an inversion-asymmetric Weyl semimetal», arXiv:2308.07408 [cond-mat.mtrl-sci].

[52] H. Bai *et al.*, «Magnetic Properties and Spin-orbit Coupling induced Semiconductivity in LK-99», arXiv:2308.05134 [cond-mat.supr-con].

[53] T. Frank *et al.*, «Copper adatoms on graphene: Theory of orbital and spin-orbital effects», *Phys. Rev. B* **95**, 035402 (2017).

[54] C.-K. Chiu, J.C.Y. Teo, A.P. Schnyder, S. Ryu, «Classification of topological quantum matter with symmetries», *Rev. Mod. Phys.* **88**, 035005 (2016).

[55] T. Hyart, R. Ojajärvi, T.T. Heikkilä, «Two Topologically Distinct Dirac-Line Semimetal Phases and Topological Phase Transitions in Rhombohedrally Stacked Honeycomb Lattices», *J. Low Temp. Phys.* **191**, 35 (2018).

[56] T. Bzdušek, M. Sigrist, «Robust doubly charged nodal lines and nodal surfaces in centrosymmetric systems», *Phys. Rev. B* **96**, 155105 (2017).

[57] A. Bouhon, A.M. Black-Schaffer, «Bulk topology of line-nodal structures protected by space group symmetries in class AI», arXiv:1710.04871 [cond-mat.mtrl-sci].

[58] Y.X. Zhao, A.P. Schnyder, Z.D. Wang, «Unified Theory of PT and CP Invariant Topological Metals and Nodal Superconductors», *Phys. Rev. Lett.* **116**, 156402 (2016).

[59] N.M. Nguyen, W. Brzezicki, T. Hyart, «Corner states, hinge states, and Majorana modes in SnTe nanowires», *Phys. Rev. B* **105**, 075310 (2022).